






Rapid Evolution of Bald Patches in a Major Solar Eruption

Jonathan H. Lee¹ , Xudong Sun (孙旭东)² , and Maria D. Kazachenko^{3,4} ¹ Institute for Astronomy, University of Hawai'i at Mānoa, 2680 Woodlawn Drive, Honolulu, HI 96822, USA² Institute for Astronomy, University of Hawai'i at Mānoa, 34 Ohia Ku Street, Pukalani, HI 96768, USA; xudongs@hawaii.edu³ Department of Astrophysical and Planetary Sciences, University of Colorado Boulder, 2000 Colorado Avenue, Boulder, CO 80305, USA⁴ National Solar Observatory, University of Colorado Boulder, 3665 Discovery Drive, Boulder, CO 80303, USA

Received 2021 September 27; revised 2021 October 18; accepted 2021 October 20; published 2021 November 3

Abstract

A bald patch (BP) is a magnetic topological feature where U-shaped field lines turn tangent to the photosphere. Field lines threading the BP trace a separatrix surface where reconnection preferentially occurs. Here we study the evolution of multiple, strong-field BPs in AR 12673 during the most intense, X9.3 flare of solar cycle 24. The central BP, located between the initial flare ribbons, largely “disintegrated” within 35 minutes. The more remote, southern BP survived. The disintegration manifested as a 9° rotation of the median shear angle; the perpendicular component of the horizontal field (with respect to the polarity inversion line) changed sign. The parallel component exhibited a step-wise, permanent increase of 1 kG, consistent with previous observations of the flare-related “magnetic imprint.” The observations suggest that magnetic reconnection during a major eruption may involve entire BP separatrices, leading to a change of magnetic topology from BPs to sheared arcades.

Unified Astronomy Thesaurus concepts: [Solar flares \(1496\)](#); [Solar magnetic reconnection \(1504\)](#); [Solar active region magnetic fields \(1975\)](#)

Supporting material: animations

1. Introduction

The coronal magnetic fields drive explosive solar activities such as flares and coronal mass ejections. As excess magnetic energy accumulates, a magnetic flux rope may form, where field lines coherently wrap around a common axis for more than one turn. The flux rope is thought to be the central engine of solar eruptions (Forbes 2000).

In the core of solar active regions (ARs), the photospheric magnetic vectors, \mathbf{B} , typically point from the positive to the negative side across the polarity inversion line (PIL). The low-lying field lines form Ω -shaped, sheared arcades that obliquely straddle the PIL. In some cases, however, they may also point from the negative to the positive side. The field lines are expected to be U-shaped and tangentially touch the photosphere at the PIL. These segments of the PIL are known as bald patches (BPs; Titov et al. 1993). BPs can occur in a variety of magnetic conditions, including quadrupolar configurations or potential fields. Shear BPs naturally occur when a magnetic flux rope lies low in the corona with its edge touching the photosphere.

Field lines threading the BP outline a separatrix surface, which is one of the magnetic topological features in the solar corona (Bungey et al. 1996). If the BP field lines are “tied” at the photospheric PIL, current sheets may form at the separatrix as a response to the boundary motions (Low & Wolfson 1988; Billinghurst et al. 1993). In reality, these field lines do not penetrate deeply into the photosphere. If the line-tying is relaxed, the BP separatrix effectively transforms into a quasi-separatrix layer (Demoulin et al. 1996). A current layer of finite width may form, and the U-shaped field lines can gradually lift up (Karpen et al. 1990, 1991).

Numerical simulations show that BPs can form during the emergence of a magnetic flux rope (Fan & Gibson 2004; Archontis et al. 2009) or during flux cancellation (van Ballegoijen & Martens 1989; Aulanier et al. 2010). Observationally, BPs can be identified in photospheric vector magnetograms. They are often found in emerging ARs (Okamoto et al. 2008; Lites et al. 2010; Kuckein et al. 2012), decaying ARs (Yardley et al. 2016), or quiet-Sun filament channels (López Ariste et al. 2006). The morphology of the X-ray sigmoids supports the existence of BPs in ARs with significant flux cancellation (Green et al. 2007; McKenzie & Canfield 2008).

Coronal field models are often used to probe the magnetic topology above BPs. Using vector magnetograms as input, these models typically recover low-lying flux ropes, just as expected (Canou et al. 2009; Guo et al. 2010; Yelles Chaouche et al. 2012; Cheng et al. 2014; Liu et al. 2014, 2019; Jiang et al. 2017). BPs have also been inferred from coronal field models that employ line-of-sight magnetograms (Delannée & Aulanier 1999; Fletcher et al. 2001; Aulanier & Schmieder 2002; Wang et al. 2002; Mandrini et al. 2002).

The photospheric magnetic fields may show rapid and permanent changes during flares (Sudol & Harvey 2005; Wang & Liu 2010; Petrie 2012; Castellanos Durán et al. 2018). These “magnetic imprints” are now frequently observed with routine, full-disk vector magnetograms such as those from the Helioseismic and Magnetic Imager (HMI; Schou et al. 2012; Hoeksema et al. 2014). The high-cadence (90 or 135 s) HMI data, in particular, have revealed a structured evolution pattern (Sun et al. 2017). In an archetypical event, the horizontal field strength B_h near the main PIL increased significantly during the earlier phase of the flare with a timescale of several minutes, while B_h in the periphery decreased at later times with smaller magnitudes and a longer timescale. A potential explanation entails Lorentz force feedback from the coronal field restructuring (Hudson 2000; Fisher et al. 2012).



Original content from this work may be used under the terms of the [Creative Commons Attribution 4.0 licence](#). Any further distribution of this work must maintain attribution to the author(s) and the title of the work, journal citation and DOI.

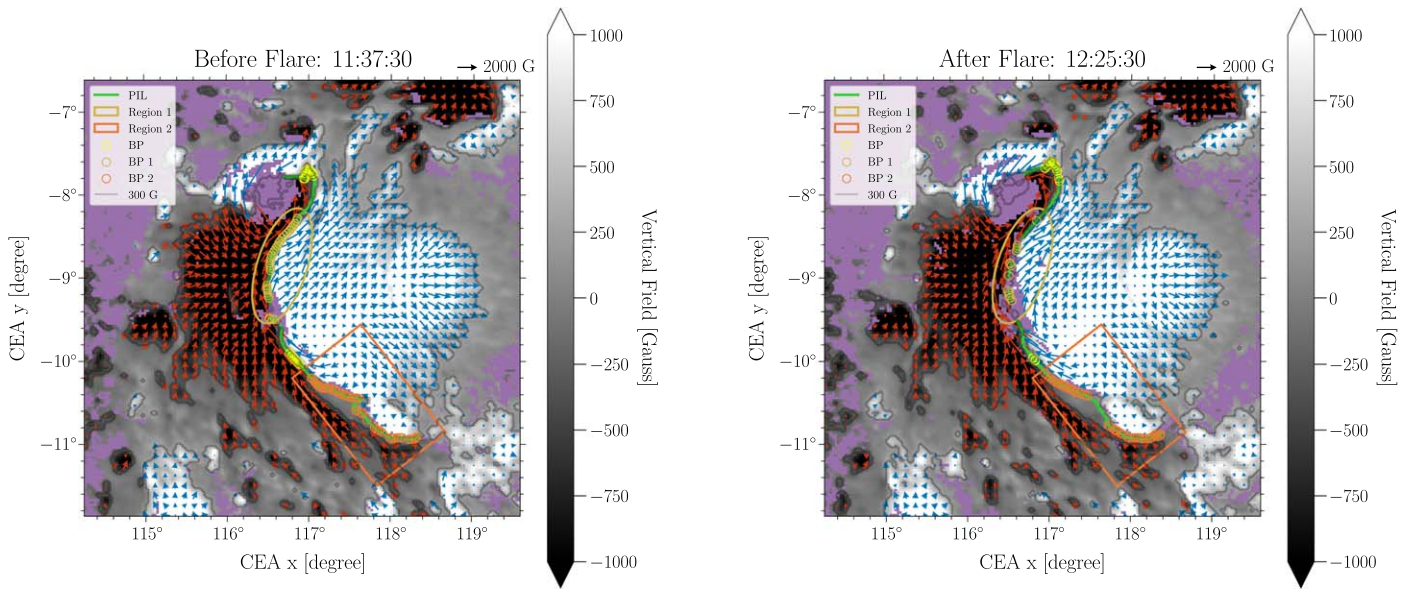


Figure 1. AR 12673 before (11:37:30 UT) and after (12:25:30 UT) the flare. The background shows the positive (negative) polarity B_z in white (black). Vectors show B_h with foot points in the positive (negative) B_z in blue (red). The PIL and BPs are shown by the green line and yellow/orange circles, respectively. The gray contour is for $B_z = 300$ G. Purple color shows pixels that are excluded from our analysis due to weaker fields or larger uncertainties. The ellipse and the box indicate our selected regions of BP evolution analysis: Region 1 for BP disintegration and Region 2 for BP survival. (An animation of this figure is available.) The animation (18 s, 88 frames) shows BP evolution from 10:49:30 UT to 13:00:00 UT. The X9.3 flare has a GOES start, peak, and end time in soft X-ray flux at 11:53 UT, 12:02 UT, and 12:10 UT, respectively. Prior to the flare, Region 1 gradually built more BPs along the PIL. Throughout the duration of the flare and afterwards, BPs in Region 1 disintegrated. BPs in Region 2 largely remained the same and survived the flare. The large amount of pixel masking occurring in the central regions of the AR and extending into both polarities during the flare is an artifact of flare ribbons, leading to many masked pixels. It can be seen in more detail in the animation corresponding to Figure 4.

(An animation of this figure is available.)

How do BPs evolve in response to a major eruption? Fan & Gibson (2007) performed magnetohydrodynamic (MHD) simulations for the eruption of a kink-unstable and a torus-unstable flux rope with BPs underneath. In the former case, the writhing motion induces internal reconnection that splits the rope vertically. As the top part escapes, the bottom part remains attached to the surface, and the BP survives. In the latter case, the expansion of the rope stretches the BP separatrix upward. Significant reconnection occurs at the BP separatrix until it finally disappears. Relevant observation, owing to the lack of high-cadence vector data, has been scarce.

NOAA AR 12673 (Figure 1) produced the most intense flare of solar cycle 24 on 2017 September 6. The GOES X9.3 flare was accompanied by a fast coronal mass ejection (Shen et al. 2018) and white-light emission (Švanda et al. 2018). Many studies have probed the coronal field structures prior to and during the eruption (Yang et al. 2017; Zou et al. 2020; Inoue & Bamba 2021). Petrie (2019) compared a pre-flare and a post-flare HMI vector magnetogram, and found clear signatures of magnetic imprints. Jiang et al. (2018) performed data-constrained MHD modeling using HMI data, the results of which will be discussed in Section 4.

Here we report on the BP evolution in AR 12673 during this major eruption. Using HMI high-cadence vector data, we quantify the rapid changes in a temporally resolved manner. Below, we describe the data and methods in Section 2, present the results in Section 3, and discuss the implications and limitations in Section 4.

2. Data and Methods

The GOES X9.3 flare (SOL2017-09-06T11:53) has start, peak, and end times in soft X-ray at 11:53 UT, 12:02 UT,

and 12:10 UT, respectively. We analyze 88 frames of HMI vector magnetograms with a 90 s cadence, which span roughly 2 hr centered around the flare peak. For each time step, we extract a 175×175 pixel map in a cylindrical equal area coordinate (Sun 2013), centered at Carrington longitude $116^\circ.9$ and latitude $-9^\circ.3$ with a $0^\circ.03$ sampling (~ 360 km). We adopt a local Cartesian approximation and decompose the field vectors as $\mathbf{B} = B_x \hat{x} + B_y \hat{y} + B_z \hat{z}$, where \hat{x} , \hat{y} , and \hat{z} are the unit vectors pointing west, north, and upward, respectively.

We use the zero vertical field contour, $B_z = 0$ G, to locate the ‘‘PIL pixels.’’ For B_z given at cell centers, the contouring routine typically returns coordinates on the cell edges. We identify the ‘‘BP pixels’’ on the PIL using the criterion (Titov et al. 1993)

$$F|_{B_z=0} = \mathbf{B}_h \cdot \nabla_h B_z|_{B_z=0} > 0, \quad (1)$$

where $\mathbf{B}_h = B_x \hat{x} + B_y \hat{y}$ is the horizontal field vector, and $\nabla_h = \partial_x \hat{x} + \partial_y \hat{y}$ represents the horizontal gradient operator. We note that $\nabla_h B_z$ is always perpendicular to the contours of B_z and points in the direction of maximal increase in B_z . This means that $\nabla_h B_z|_{B_z=0}$ is perpendicular to the PIL, i.e., the $B_z = 0$ contour, pointing from negative to positive polarity. Hereafter, we assume the subcell values are bilinear, consistent with the contouring routine.

We calculate the following variables of interest for the PIL pixels: the horizontal field strength (B_h), the parallel component of \mathbf{B}_h with respect to the PIL (B_h^\parallel), the corresponding, perpendicular component (B_h^\perp), and the magnetic shear angle (θ_s). They are defined as follows:

$$B_h = (B_x^2 + B_y^2)^{1/2}, \quad (2)$$

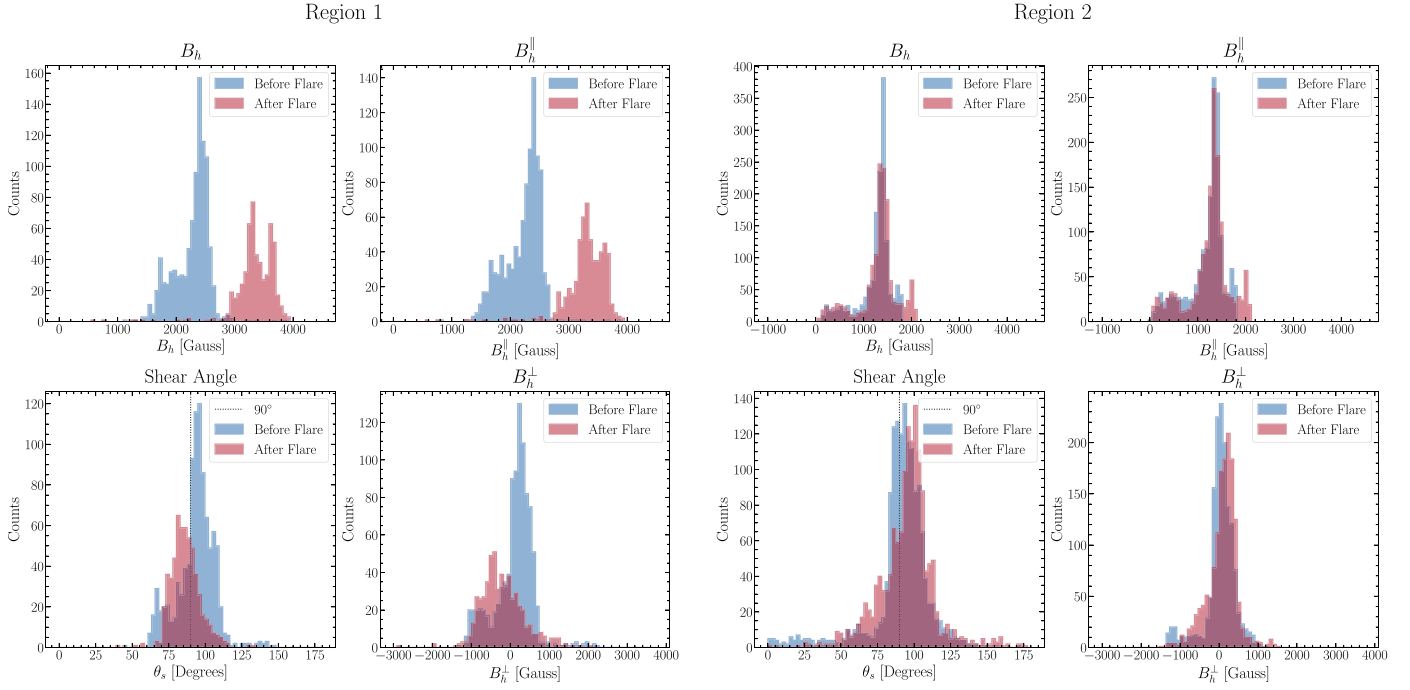


Figure 2. Distributions of B_h , B_h^{\parallel} , B_h^{\perp} , and θ_s for 17 combined time steps before (blue, 11:27–11:51 UT) and after (red, 12:12–12:36 UT) the flare at the PIL pixels in Region 1 (left) and Region 2 (right). The vertical dotted line is for $\theta_s = 90^\circ$.

$$B_h^{\perp} = B_h \cdot \frac{\nabla_h B_z}{\|\nabla_h B_z\|}, \quad (3)$$

$$B_h^{\parallel} = [B_h^2 - (B_h^{\perp})^2]^{1/2}, \quad (4)$$

$$\theta_s = 180^\circ - \arccos \frac{B_h \cdot \nabla_h B_z}{\|B_h\| \|\nabla_h B_z\|}. \quad (5)$$

In our convention, B_h^{\perp} is positive for BPs, and negative otherwise. The shear angle θ_s is zero if \mathbf{B} is perpendicular to the PIL and points from the positive to the negative polarity. Sheared arcades have $0^\circ < \theta_s < 90^\circ$; BPs have $\theta_s > 90^\circ$. We do not consider B_z as all analyses are restricted to the PIL pixels, where $B_z = 0$ G is satisfied to machine accuracy.

Following Avallone & Sun (2020), we use a Monte Carlo method to estimate the statistical uncertainties. A random sample ($N = 100$) is drawn for \mathbf{B} at each pixel in the full-disk magnetogram based on the variances and covariances provided by the HMI pipeline. It is then used to calculate a sample of the desired variables. The 1σ confidence interval is finally quoted.

For analysis, we exclude those pixels with weaker field strength, $\|\mathbf{B}\| < 200$ G, as they have relatively higher noises. Several subregions in AR 12673 exhibit particularly large uncertainties, including the sunspot umbra in the north, the δ -penumbra at the center, and the flare ribbons. We identify and exclude them by imposing an empirical threshold (two standard deviations above the median) on the statistical uncertainties of the three field components: $\sigma_{B_x} > 162$ G, $\sigma_{B_y} > 152$ G, and $\sigma_{B_z} > 135$ G. We further discuss the uncertainties in Section 4.

Using the flare ribbon information from the RibbonDB database (Kazachenko et al. 2017) derived from the Atmospheric Imaging Assembly (Lemen et al. 2012) 1600 Å images, we locate all the pixels that have risen above 8 times the median image intensity up to the time of interest. We consider them as the foot points of the field lines that have reconnected, and integrate the corresponding HMI B_z pixels to

estimate the accumulated reconnecting magnetic flux Φ :

$$\Phi = \int |B_z| d S_{\text{ribbon}}, \quad (6)$$

where S_{ribbon} denotes the accumulated ribbon area. Equation (6) includes both positive and negative fluxes. Different thresholds for the ribbon brightness, i.e., 6 and 10 times the median, are used for the uncertainty estimate.

3. Result

AR 12673 hosted a complex $\beta\gamma\delta$ -class sunspot group prior to the eruption. The coronal loops in the core region have an inverse-S shape. This suggests that the coronal fields have left-handed twist, consistent with the result from magnetic extrapolation (e.g., Wang et al. 2018).

For each time step, we calculate F with Equation (1) and other variables of interest for all the PIL pixels with low statistical uncertainty. We select two subregions, Regions 1 and 2 (Figure 1), for further analysis. We exclude the data taken during the flare (12:12–12:36 UT), because the flare emission creates a significant transient signal at ribbon loci (see Section 4).

For Region 1 at the central portion of the PIL, 73% of pixels (43 out of 59) have $F > 0$ at 11:37:30 UT (pre-flare) and are identified as BP. This is in sharp contrast with the 12:25:30 UT (post-flare) frame, where only 39% of pixels (14 out of 36) are identified as BP. As directly discernible in Figure 1, the BP appears to have “disintegrated” during the eruption. For Region 2 at the southern portion of the PIL, 63% of pixels (55 out of 87) are identified as BPs pre-flare, and 71% of pixels (57 out of 80) post-flare. The BP appears to have survived the eruption.

The distributions of several variables of interest are shown in Figure 2. In Region 1, both B_h and B_h^{\parallel} greatly increased after the flare; the median increase is 988 G for B_h and 1024 G for B_h^{\parallel} . The significant increase is in line with previous findings of the

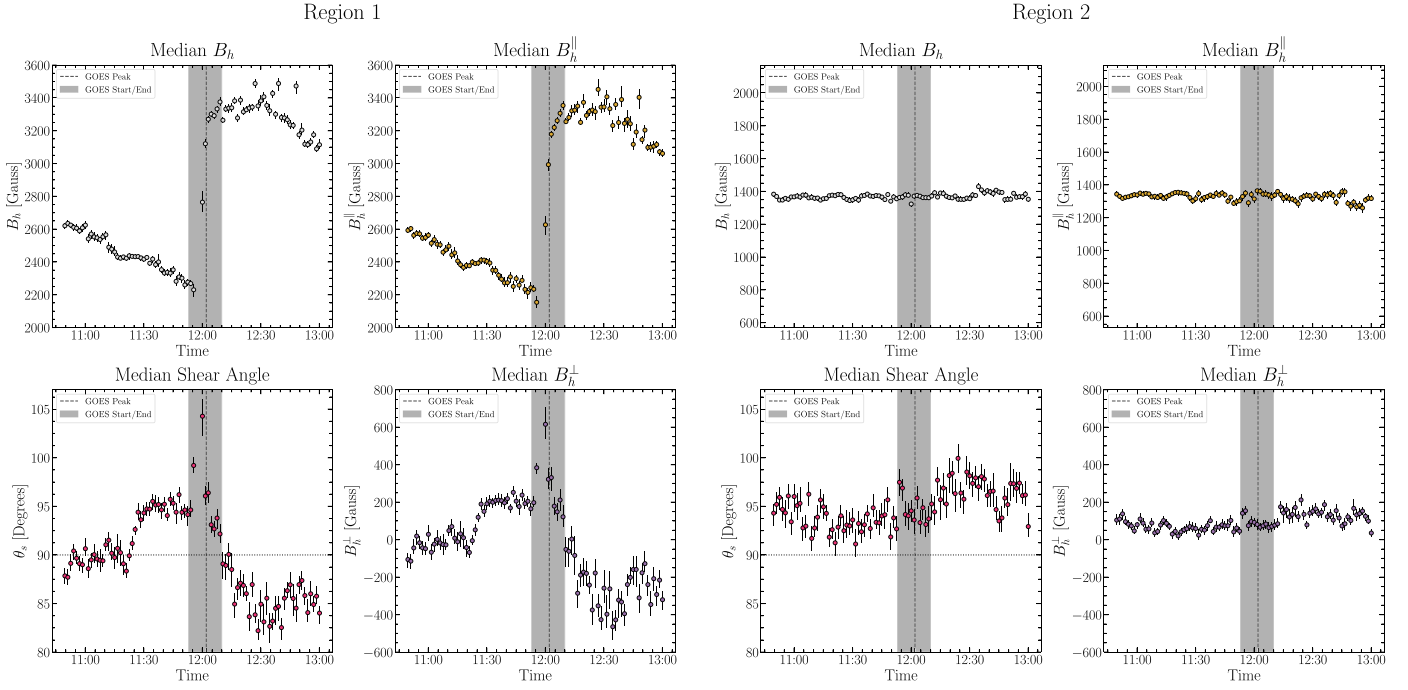


Figure 3. Time series of median B_h , B_h^{\parallel} , B_h^{\perp} , and θ_s at PIL pixels in Region 1 (left) and Region 2 (right). The error bars show the 1σ confidence interval of the median derived from the Monte Carlo method. The vertical gray bar (dotted line) shows the flare duration (peak time). The horizontal dotted line is for $\theta_s = 90^\circ$.

magnetic imprints. In contrast, B_h^{\perp} reversed sign; its median changed from 201 to -262 G. The median θ_s decreased by 9° , from 95° to 86° . In Region 2, most pixels had $B_h^{\perp} > 0$ G and $\theta_s > 90^\circ$ both before and after the flare. The median changes before to after the flare are 9 G, 3 G, 79 G, and 4° for B_h , B_h^{\parallel} , B_h^{\perp} , and θ_s , respectively.

We conduct a two-sample Kolmogorov–Smirnov (K-S) test to evaluate whether the pre- and post-flare variables are likely drawn from the same distribution. The K-S D statistics for Region 2 are 3–10 times smaller than those of Region 1. Nevertheless, the p values for all four variables are small ($p < 10^{-6}$) in both subregions, which indicates some differences between the pre- and post-flare states.

The temporal profiles of the median values are shown in Figure 3. As expected, Region 1 exhibited a rapid and permanent increase of roughly 1 kG in B_h during the flare, which mostly comes from B_h^{\parallel} . Interestingly, the median B_h^{\perp} (θ_s) increased from about 0 G (90°) to 200 G (95°) between 11:20 UT and 11:35 UT, suggesting rapid formation of new BPs. Their values subsequently decreased after the flare onset, which caused the apparent BP disintegration. In comparison, the temporal variations in Region 2 were much smaller.

We show the flare ribbon evolution in Figure 4 and the estimated reconnection flux Φ in Figure 5. At the flare onset, the ribbons first appeared close to the northern portion of the PIL, including Region 1 (left panel of Figure 4). This suggests that the BP separatrix in Region 1 may have participated in the flare reconnection early on, when the reconnection flux rate $d\Phi/dt$ was near its maximum, 8.11×10^{19} Mx s $^{-1}$. The ribbons subsequently extended along the PIL to cover Region 2 (right panel), when $d\Phi/dt$ was much reduced, 3.72×10^{19} Mx s $^{-1}$. Meanwhile, the ribbons also moved away from the PIL, suggesting that the coronal reconnection proceeded to higher altitudes. The evolution pattern is typical for two-ribbon flares (Qiu 2009).

4. Discussion

Our observations show that a segment of BP in AR 12673 rapidly disintegrated during the X9.3 flare. The apparent disintegration is a consequence of the changing B_h^{\perp} and θ_s , as the local magnetic azimuth angles rotated by about 10° over half an hour. The post-flare B_h pointed from the positive to the negative polarity, and the low-lying field lines assumed a sheared arcade topology instead. The rotation is reminiscent of a 12° permanent rotation of a sunspot (Liu et al. 2016) and a 12° – 20° transient rotation of photospheric fields (Xu et al. 2018) during flares.

Our observations also show that the parallel component of the horizontal field increased by about 1 kG, in line with previous reports of magnetic imprint. This is consistent with the findings of Petrie (2019) on Region 1.

The morphological evolution of the flare ribbons contains rich information about the coronal reconnection processes. During the early phase of the flare, the ribbons extended along and moved away from the PIL. The extension is approximately centered at Region 1; it is mainly northward (southward) in the negative (positive) polarity, manifesting the sheared component of the reconnecting fields (Qiu 2009). The outward motion away from the PIL indicates that the reconnection occurs at progressively higher altitude, and starts to involve the overlying fields. We note that the ribbon evolution after the flare peak was rather complex, with possible inward motions toward the PIL near Region 1. Given the multipolar nature of AR 12673 and the possible multi-flux-rope eruption (Hou et al. 2018), the peculiar motion may be a consequence of breakout-type reconnection (e.g., Lynch & Edmondson 2013; Dahlin et al. 2019). A detailed analysis is deferred to future work.

In Fan & Gibson (2007), the BP separatrix disappears due to intense reconnection that proceeds to very low altitudes. Our observations appear to be consistent with the scenario, especially when the contrasting behaviors of Regions 1 and

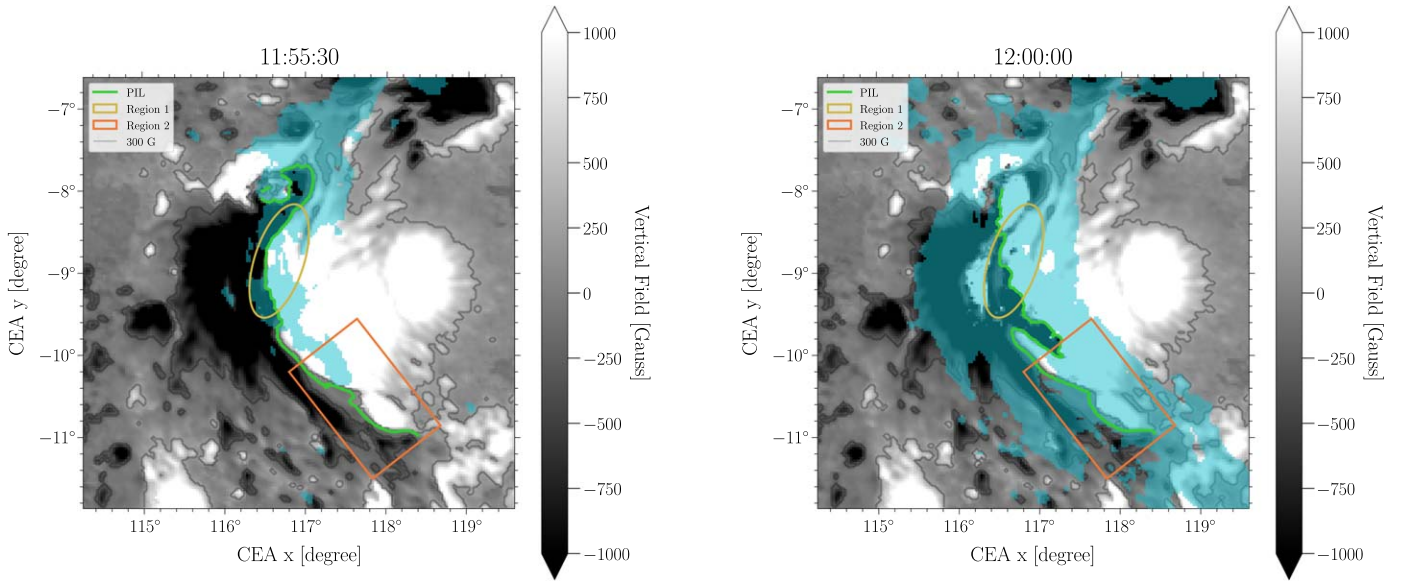


Figure 4. AIA 1600 Å flare ribbons in teal during the flare onset (left, 11:55:27 UT) and shortly before the flare peak (right, 12:00:15 UT). (An animation of this figure is available.) The animation (18 s, 88 frames) shows the flare ribbon evolution from 10:49:30 UT to 13:00:00 UT. During the onset of eruption, ribbons developed along the PIL within Region 1 and exterior to the PIL in Region 2. Prior to the flare peak, flare ribbons propagated along and separated away from the PIL covering the entirety of Region 1 and Region 2.

(An animation of this figure is available.)

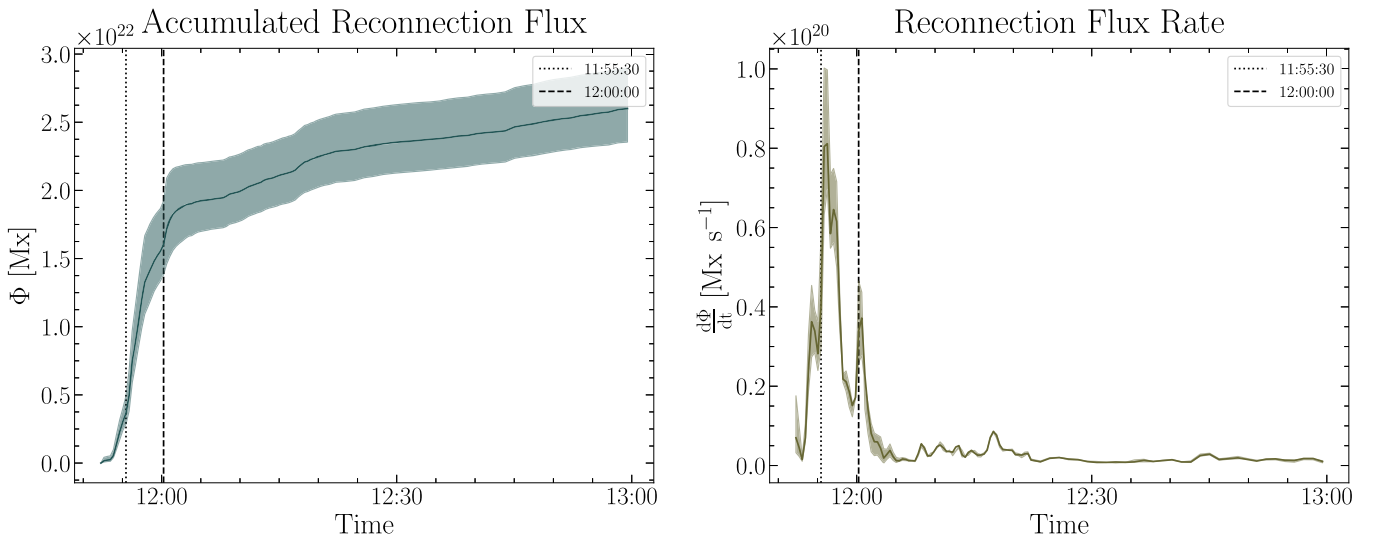


Figure 5. Left: accumulated reconnection flux Φ . Right: reconnection flux rate $d\Phi/dt$. The vertical dotted and dashed lines indicate the two times shown in Figure 4.

2 are taken into account. The early, more intense reconnection likely occurred at a lower altitude above Region 1. It may have involved the entire BP separatrix, leading to the rapid disintegration of the BP there. Region 2 was involved later when the reconnection proceeded to higher altitudes, as suggested by the separation of the ribbons away from the PIL. The BP separatrix there was less involved, and the BP survived. Indeed, photospheric white-light flare ribbons were observed by HMI, and the 10–25 keV hard X-ray kernels were observed by the RHESSI satellite (Yang et al. 2017; Romano et al. 2019). Both appeared near Region 1 only and are indicative of intense magnetic reconnection.

Jiang et al. (2018) extrapolate a nonlinear force-free field from HMI vector data as the initial state of their MHD simulation. The pre-eruption coronal field contains a low-lying

flux rope right above the BP in Region 1. The small residual Lorentz force in the extrapolation model provides the initial disturbance; plasma instability eventually leads to a full eruption. Similar to Fan & Gibson (2007), an intense current sheet forms at the stretched BP separatrix, which is eventually converted into sheared arcades. The ribbon motions during the early stage of the flare, i.e., extension along and expansion away from the PIL, are well reproduced in the model. Even though the photospheric B_h is not observationally constrained in the numerical simulation of Jiang et al. (2018) for AR 12673, the simulated BP evolution appears to match the HMI data qualitatively, including a clear increase in the strength of the horizontal field, B_h (C. Jiang 2021, private communication).

We note that many previous observational and modeling studies (Section 1) have discussed BP separatrix reconnection,

though mostly in less energetic contexts such as $H\alpha$ surges or confined flares. The photospheric field changes in those events remain to be studied, but are likely less drastic.

We finally comment on the uncertainties. First, the δ -penumbra at the southern section of Region 1 (centered at $(116^\circ.5, -9^\circ.5)$ in Figure 1) consistently shows high statistical errors, therefore, reducing the number of PIL pixels considered for analysis. The cause may be the combined effect of extremes in the Doppler velocity and limitations of the magnetic inference technique. Second, the average σ_{B_x} , σ_{B_y} , and σ_{B_z} in pixels where $\|\mathbf{B}\| > 200$ G increased by 36 G, 26 G, and 30 G, respectively, post-flare, leading to a reduced number of pixels available for analysis. The increase mainly originates from the northern umbra and the δ -penumbra, the reason for which is unclear. The regions swept by the flare ribbons, on the other hand, have similar uncertainty as the surrounding regions in the post-flare frames. Third, flare emission in ribbons is known to cause transient artifacts in photospheric magnetograms such as sign reversals (Qiu & Gary 2003; Sun et al. 2017). The effect clearly manifests in the right panel of Figure 4 as parasitic polarities that distort the PIL. They are also visible in the animation of Figures 1 and 4. Fourth, the determination of the BP relies on the resolution of the 180° ambiguity of the magnetic azimuth. The HMI pipeline algorithm (Leka et al. 2009) includes the divergence-free constraint, which has been shown to work well in several theoretical cases with BPs (Li et al. 2007). Additional constraints come from the inverse-S-shaped sigmoids observed in the corona, which is consistent with the negative helicity inferred from the photosphere vector field. Finally, flare ribbon observations in 1600 \AA are subject to saturation during larger flares. The associated “blooming” effect, where the saturation causes excess charge to spread to neighboring pixels on the detector, can lead to an overestimate of the ribbon area and the absolute values of the reconnection flux rates. Diffraction patterns from the AIA entrance filter may also affect the result.

We thank Chaowei Jiang for helpful discussions. J.L. and X.S. are supported by NSF awards #1848250 and #1854760, and the state of Hawai‘i. M.D.K. acknowledges support from NASA ECIP award NNH18ZDA001N. The SDO data are courtesy of NASA, the HMI, and the AIA science teams.

Facility: SDO.

ORCID iDs

Jonathan H. Lee  <https://orcid.org/0000-0001-7626-8386>

Xudong Sun (孙旭东)  <https://orcid.org/0000-0003-4043-616X>

Maria D. Kazachenko  <https://orcid.org/0000-0001-8975-7605>

References

- Archontis, V., Hood, A. W., Savcheva, A., Golub, L., & Deluca, E. 2009, *ApJ*, **691**, 1276
- Aulanier, G., & Schmieder, B. 2002, *A&A*, **386**, 1106
- Aulanier, G., Török, T., Démoulin, P., & DeLuca, E. E. 2010, *ApJ*, **708**, 314
- Avallone, E. A., & Sun, X. 2020, *ApJ*, **893**, 123
- Billingham, M. N., Craig, I. J. D., & Sneyd, A. D. 1993, *A&A*, **279**, 589
- Bungey, T. N., Titov, V. S., & Priest, E. R. 1996, *A&A*, **308**, 233
- Canou, A., Amari, T., Bommier, V., et al. 2009, *ApJL*, **693**, L27
- Castellanos Durán, J. S., Kleint, L., & Calvo-Mozo, B. 2018, *ApJ*, **852**, 25
- Cheng, X., Ding, M. D., Zhang, J., et al. 2014, *ApJ*, **789**, 93
- Dahlin, J. T., Antiochos, S. K., & DeVore, C. R. 2019, *ApJ*, **879**, 96
- Delannée, C., & Aulanier, G. 1999, *SoPh*, **190**, 107
- Démoulin, P., Priest, E. R., & Lonie, D. P. 1996, *JGR*, **101**, 7631
- Fan, Y., & Gibson, S. E. 2004, *ApJ*, **609**, 1123
- Fan, Y., & Gibson, S. E. 2007, *ApJ*, **668**, 1232
- Fisher, G. H., Bercik, D. J., Welsch, B. T., & Hudson, H. S. 2012, *SoPh*, **277**, 59
- Fletcher, L., López Fuentes, M. C., Mandrini, C. H., et al. 2001, *SoPh*, **203**, 255
- Forbes, T. G. 2000, *JGR*, **105**, 23153
- Green, L. M., Kliem, B., Török, T., van Driel-Gesztelyi, L., & Attrill, G. D. R. 2007, *SoPh*, **246**, 365
- Guo, Y., Schmieder, B., Démoulin, P., et al. 2010, *ApJ*, **714**, 343
- Hoeksema, J. T., Liu, Y., Hayashi, K., et al. 2014, *SoPh*, **289**, 3483
- Hou, Y. J., Zhang, J., Li, T., Yang, S. H., & Li, X. H. 2018, *A&A*, **619**, A100
- Hudson, H. S. 2000, *ApJL*, **531**, L75
- Inoue, S., & Bamba, Y. 2021, *ApJ*, **914**, 71
- Jiang, C., Zou, P., Feng, X., et al. 2018, *ApJ*, **869**, 13
- Jiang, C.-W., Feng, X.-S., Wu, S.-T., & Hu, Q. 2017, *RAA*, **17**, 093
- Karpen, J. T., Antiochos, S. K., & DeVore, C. R. 1990, *ApJL*, **356**, L67
- Karpen, J. T., Antiochos, S. K., & DeVore, C. R. 1991, *ApJ*, **382**, 327
- Kazachenko, M. D., Lynch, B. J., Welsch, B. T., & Sun, X. 2017, *ApJ*, **845**, 49
- Kuckein, C., Martínez Pillet, V., & Centeno, R. 2012, *A&A*, **539**, A131
- Leka, K. D., Barnes, G., Crouch, A. D., et al. 2009, *SoPh*, **260**, 83
- Lemen, J. R., Title, A. M., Akin, D. J., et al. 2012, *SoPh*, **275**, 17
- Li, J., Amari, T., & Fan, Y. 2007, *ApJ*, **654**, 675
- Lites, B. W., Kubo, M., Berger, T., et al. 2010, *ApJ*, **718**, 474
- Liu, C., Xu, Y., Cao, W., et al. 2016, *NatCo*, **7**, 13104
- Liu, L., Cheng, X., Wang, Y., & Zhou, Z. 2019, *ApJ*, **884**, 45
- Liu, R., Titov, V. S., Gou, T., et al. 2014, *ApJ*, **790**, 8
- López Ariste, A., Aulanier, G., Schmieder, B., & Sainz Dalda, A. 2006, *A&A*, **456**, 725
- Low, B. C., & Wolfson, R. 1988, *ApJ*, **324**, 574
- Lynch, B. J., & Edmondson, J. K. 2013, *ApJ*, **764**, 87
- Mandrini, C. H., Démoulin, P., Schmieder, B., Deng, Y. Y., & Rudawy, P. 2002, *A&A*, **391**, 317
- McKenzie, D. E., & Canfield, R. C. 2008, *A&A*, **481**, L65
- Okamoto, T. J., Tsuneta, S., Lites, B. W., et al. 2008, *ApJL*, **673**, L215
- Petrie, G. J. D. 2012, *ApJ*, **759**, 50
- Petrie, G. J. D. 2019, *ApJS*, **240**, 11
- Qiu, J. 2009, *ApJ*, **692**, 1110
- Qiu, J., & Gary, D. E. 2003, *ApJ*, **599**, 615
- Romano, P., Elmhamdi, A., & Kordi, A. S. 2019, *SoPh*, **294**, 4
- Schou, J., Scherrer, P. H., Bush, R. I., et al. 2012, *SoPh*, **275**, 229
- Shen, C., Xu, M., Wang, Y., Chi, Y., & Luo, B. 2018, *ApJ*, **861**, 28
- Sudol, J. J., & Harvey, J. W. 2005, *ApJ*, **635**, 647
- Sun, X. 2013, arXiv:1309.2392
- Sun, X., Hoeksema, J. T., Liu, Y., Kazachenko, M., & Chen, R. 2017, *ApJ*, **839**, 67
- Švanda, M., Jurčák, J., Kašparová, J., & Kleint, L. 2018, *ApJ*, **860**, 144
- Titov, V. S., Priest, E. R., & Démoulin, P. 1993, *A&A*, **276**, 564
- van Ballegoijen, A. A., & Martens, P. C. H. 1989, *ApJ*, **343**, 971
- Wang, H., & Liu, C. 2010, *ApJL*, **716**, L195
- Wang, R., Liu, Y. D., Hoeksema, J. T., Zimovets, I. V., & Liu, Y. 2018, *ApJ*, **869**, 90
- Wang, T., Yan, Y., Wang, J., Kurokawa, H., & Shibata, K. 2002, *ApJ*, **572**, 580
- Xu, Y., Cao, W., Ahn, K., et al. 2018, *NatCo*, **9**, 46
- Yang, S., Zhang, J., Zhu, X., & Song, Q. 2017, *ApJL*, **849**, L21
- Yardley, S. L., Green, L. M., Williams, D. R., et al. 2016, *ApJ*, **827**, 151
- Yelles Chaouche, L., Kuckein, C., Martínez Pillet, V., & Moreno-Insertis, F. 2012, *ApJ*, **748**, 23
- Zou, P., Jiang, C., Wei, F., et al. 2020, *ApJ*, **890**, 10